International Journal of Rock Mechanics & Mining Sciences 65 (2014) 116–128

Contents lists available at ScienceDirect

International Journal of Rock Mechanics & Mining Sciences

journal homepage: www.elsevier.com/locate/ijrmms

An improved numerical manifold method for simulation of sequential excavation in fractured rocks

Yuval Tal [a], Yossef H. Hatzor [a,b,*], Xia-Ting Feng [b]

[a] Department of Geological and Environmental Sciences, Ben-Gurion University of the Negev, Beer-Sheva 84105, Israel
[b] State Key Laboratory of Geomechanics and Geotechnical Engineering, Institute of Rock and Soil Mechanics, Chinese Academy of Sciences, Wuhan 430071, People's Republic of China

ARTICLE INFO

Article history:
Received 24 October 2012
Received in revised form
17 May 2013
Accepted 10 October 2013
Available online 28 November 2013

Key words:
Discrete element modeling
Numerical manifold method
In situ stresses
Excavation sequence
Jinping hydroelectric project

ABSTRACT

We improve the original numerical manifold method (NMM) capability to correctly model the stability of underground openings embedded in discontinuous rock masses under high *in situ* stress conditions by implementing an algorithm which models the excavation sequence during NMM simulations, starting with a domain with no opening at all and progressively adding openings according to the planned construction phases. The significance of this improvement is demonstrated using the case of Zedekiah cave underneath the old city of Jerusalem, excavated 2000 years ago at a shallow depth in a highly discontinuous rock mass and still stands unsupported. The results clearly show that modeling underground openings in discontinuous rocks without consideration of the excavation sequence is overly conservative. We proceed with developing a new procedure to impose high initial stresses in NMM for accurate deformation modeling of deep underground excavations, and verify our suggested approach using the analytical Kirsch solution. Finally, we apply our enhanced NMM code to the Jinping hydroelectric project tunnels in Sichuan Province, China. Using very accurate sliding micrometer data obtained during the excavation of a research tunnel within the Jinping tunnel complex we constrain the *in situ* stress field at depth by inversion of the measured displacement data using the modified NMM code. The results provide a quantitative assessment of the *in situ* stress field in Jinping tunnels at a depth of 2525 m below ground surface, where the execution of *in situ* stress measurements by conventional procedures proves an extremely challenging task.

1. Introduction

In this paper, we present several important enhancements to the numerical manifold method (NMM) originally proposed by Shi [1], and apply those enhancement to perform stress inversion based on accurate sliding micrometer data obtained *in situ* at the 2525 m deep Jinping tunnels located in Sichuan province, China.

The NMM inherits the strengths of the numerical, discrete element, discontinuous deformation analysis (DDA) method proposed earlier by Shi [2] for block kinematics analysis, and retains its excellent contact detection algorithm, its unique open-close iteration procedure that guarantees that at the end of every time step there is no tension and no penetration between discrete blocks, and its fully dynamic formulation. Both DDA and NMM can therefore deal with the mechanical response of a block system under general loading and moving boundary conditions when body movement and large deformation occur simultaneously. But in addition, the NMM incorporates a mathematical cover over the DDA block system thus enabling accurate calculation of stress and strain distributions within block elements as well as everywhere else in the analysis domain. Therefore, when the displacement of the blocky rock mass is of concern, DDA can be used safely and can be trusted to provide accurate results, both for static and dynamic cases, as has been shown in multitude validation and verification studies [3] and can be effectively applied for underground engineering [4–8]. However, when accurate stress or strain distribution in a discontinuous domain is sought the NMM will provide much more accurate results, particularly when the blocks are large with respect to the modeled domain dimensions, due to DDA's simply deformable blocks assumption. The NMM can be viewed, therefore, as a natural bridge between the continuum and discrete representations, by combining the DDA and FEM methods in a united form [9]. The essentials of the numerical manifold methods are discussed by many authors [10–14] and will not be repeated here, for brevity.

Previous NMM research has mainly focused on theoretical implementations and improvements of the NMM rather than

* Corresponding author at: Department of Geological and Environmental Sciences, Ben-Gurion University of the Negev, Beer-Sheva 84105, Israel. Tel.: +972 8 647 2621; fax: +972 8 642 8717.
E-mail address: hatzor@bgu.ac.il (Y.H. Hatzor).

1365-1609/$ - see front matter © 2013 Elsevier Ltd. All rights reserved.
http://dx.doi.org/10.1016/j.ijrmms.2013.10.005

application to real case studies. The main developments of the NMM can be categorized into three groups: (1) improvement of the approximation accuracy [10,11]; (2) extension of the NMM for crack propagation problems [14–16]; and (3) development of 3D NMM [12,13,17]. An important limitation of the original NMM code when applied to underground mining is that in the original program developed by Shi [1], and also in the original DDA code [2], the excavation is open from the beginning of the simulation—before the stresses have reached their ultimate value everywhere in the modeled domain. It has been shown [18] that the number of time steps it takes for the stresses to attain their theoretical value everywhere in the modeled domain increases with the increasing number of blocks in the mesh. In reality, however, when tunnels are excavated, initial compressive stresses have already developed to their full extent in the rock mass, and the rock column has already experienced elastic deformation over geologic times under the overburden and tectonic stresses. Realizing this is important when analyzing the stability of underground openings in discontinuous rock masses using DDA or NMM as ignoring this numerical artifact may lead to overly conservative design. We demonstrate the significance of modeling sequential excavation using a real case study of a historic 40 m span cavern which was excavated more than 2000 years ago underneath the old city of Jerusalem and still stands unsupported.

Another important issue which is addressed in this paper is how to correctly impose the initial *in situ* stresses with NMM when analyzing deep tunnels. We discovered that with the available "initial stresses" option in the original NMM code the specified initial stresses are dissipated in the course of the simulation and are not maintained at their original value before the excavation material has been removed by means of the new sequential excavation algorithm. This could be the result of a numerical artifact possibly associated with the contact algorithm in the original NMM code which may be improved in the future as the method matures. At present we overcome this problem by applying tractions on the boundaries of the modeled domain in addition to the existing "initial stress" option thus imposing the desired initial stresses on the modeled domain. The detailed procedure for imposing initial stresses in NMM using tractions on the boundaries is described and verified in this paper.

Finally, our enhanced NMM code, with imposed initial stresses and sequential excavation algorithm, is applied to the case of the Jinping hydroelectric project in China in order to find the best fit *in situ* stresses at the site by inversion of accurate sliding micrometer data obtained at the site during tunnel excavation.

2. Simulating the excavation sequence with NMM

In the original NMM underground openings are modeled as an existing cavity in the mesh from the first time step and throughout the simulation. It has been observed by many researchers however [e.g. [19]] that gravity is not immediately "turned on", both in DDA and in NMM, and so the numerical values of the stresses at a given depth in the mesh approach the theoretical value only after a significant number of time steps has elapsed, the number of which has been shown to increase with the increasing number of blocks in the mesh [18]. Naturally, the theoretically available frictional resistance across the discontinuities, defined by the assigned friction angle and the level of normal stress acting on the joints, is not fully mobilized until gravity is completely turned on and the stresses acting on the joints attain their ultimate magnitude. Consequently, blocks that are free to move from the rock mass into the excavation space from a kinematical stand point will tend to do so from the first time step of the simulation, when the frictional resistance is much lower than the theoretical level. This will obviously lead to exaggerated block displacements and as a result to overly conservative design.

The original NMM code is modified here to enable modeling tunnel excavation during the NMM simulation after the initial stresses are fully developed and the corresponding elastic deformation has already taken place. The modified NMM code contains two stages: (1) at the beginning of the simulation a single or few blocks replace the tunnel and "static" simulation (in a "static" simulation the initial velocity at the beginning of every time step is set to zero everywhere in the domain) is executed until equilibrium is attained. Then, (2) the tunnel blocks are removed so as to simulate tunnel excavation, and a "dynamic" or "static" computation is executed (in a "dynamic" simulation the terminal velocity in the previous time step is inherited in the new time step everywhere in the domain). Here the excavation sequence is not modeled by reducing the elastic constants (e.g. Young's modulus, Poisson's ratio) or by assigning zero stress in all elements inside the tunnel, because blocks that are free from a kinematical stand point to fall into the tunnel space may cause numerical instabilities when in contact with tunnel elements having zero or very small stiffness. A procedure to overcome this difficulty by introducing a softening block approach has been suggested recently [20].

The block removal process requires careful preprocessing at every excavation sequence which includes the removal of manifold elements inside every block that is to be removed and their corresponding star nodes, as well as the detachment of contacts

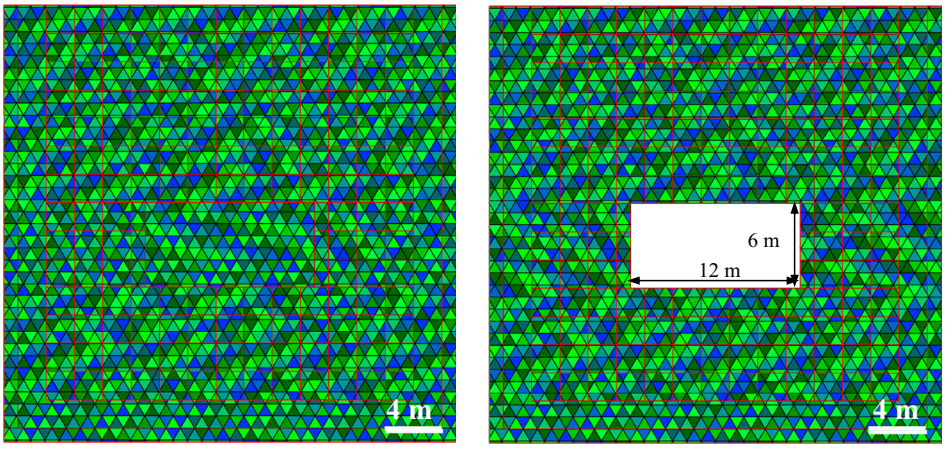

Fig. 1. NMM model for testing the significance of the proposed sequential excavation algorithm: modified (left) and original (right) NMM model at the beginning of the simulation.

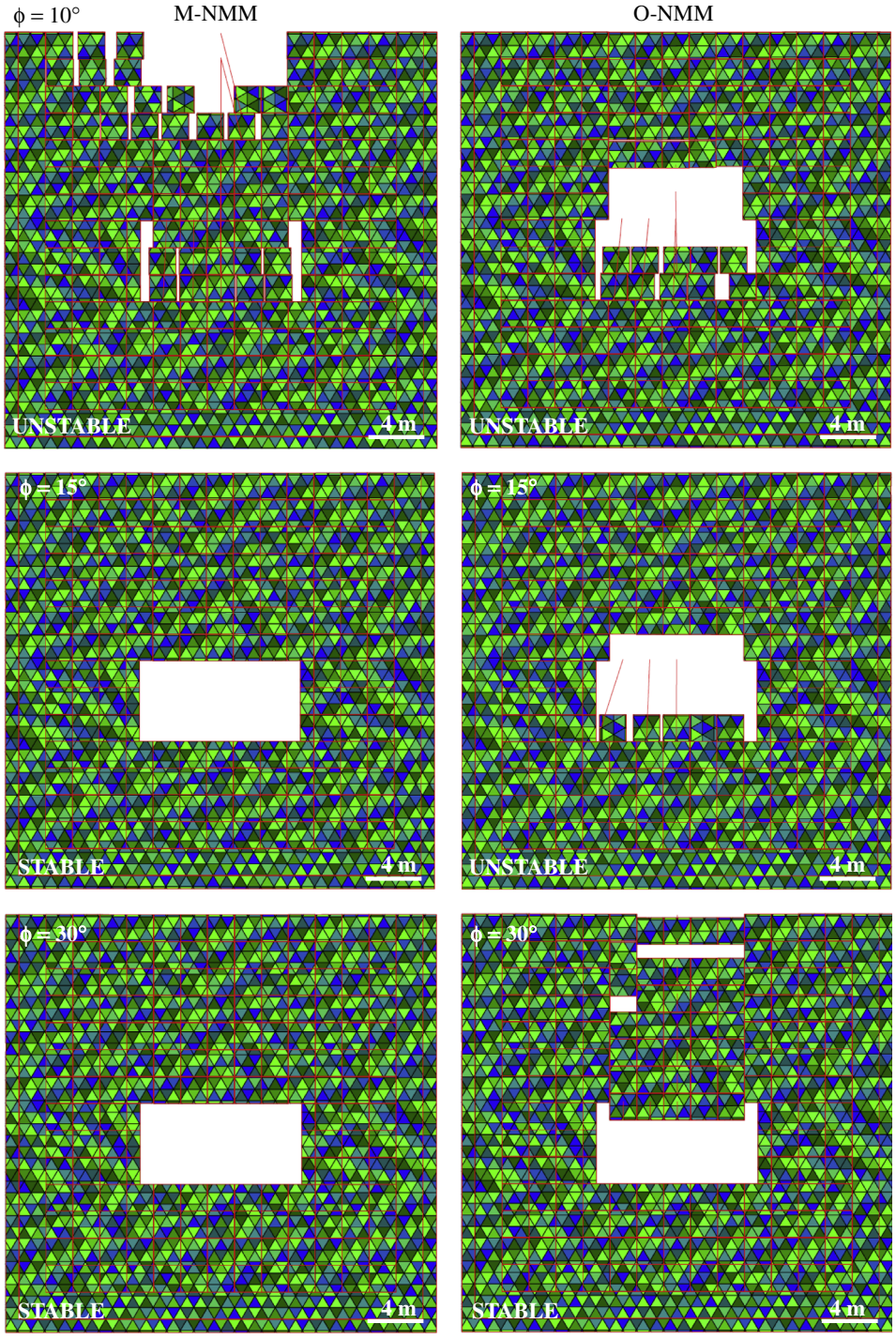

Fig. 2. Graphic output of forward modeling with modified (left panels) and original (right panels) NMM for the model shown in Fig. 1 with discontinuity friction angle of 10º, 15º, and 30º.

with neighboring blocks while keeping the contacts between the remaining blocks. Because manifold elements are the intersection between the physical domain and the mathematical cover, the removal of an existing block enables realistic modeling of the excavation sequence without splitting existing manifold elements.

In order to compare the evolution of deformation with the modified NMM where the underground opening is excavated during the simulation, and the original NMM where the opening exists from the beginning of the simulation, seven simulations with discontinuity friction angle of 10°, 15°, 20°, 25°, 30°, 35° and 40° are performed for a theoretical opening shown in Fig. 1 with each method, and snapshots of the obtained deformation patterns for friction angles 10º, 15°, and 30º are shown in Fig. 2. Inspection of Fig. 2 reveals that with discontinuity friction angle of $\phi = 10^\circ$ the opening is not stable when analyzed with both approaches. With discontinuity friction angle of $\phi = 15^\circ$ the opening is not stable with the original NMM but is stable with the modified NMM. With friction angles $\phi = 30^\circ$ and above the opening is stable when analyzed with both approaches. Clearly, therefore, performing the simulation with the original NMM code would lead to a significant underestimation of the required discontinuity friction

angle for stability. Performing the analysis with the modified NMM indicates that the required discontinuity friction angle for stability for the model geometry in Fig. 1 is $\phi=15^{\circ}$ whereas with the original NMM the required discontinuity friction angle for stability would be $\phi=30^{\circ}$.

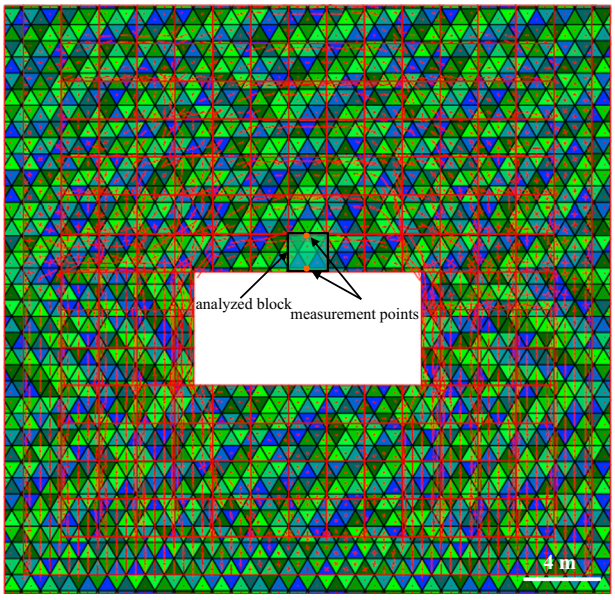

Fig. 3. Result of modified NMM at the end of the simulation with the location of the analyzed block and two measurement points. Principal stress trajectories delineated in red. $\phi=30^{o}$ at all discontinuities. (For interpretation of the references to color in this figure caption, the reader is referred to the web version of this paper.)

To demonstrate the power of NMM to perform stress distribution analysis within a single block in a jointed domain consider Fig. 3 where the final stress configuration obtained with modified NMM is shown for a discontinuity friction angle of $\phi=30^{\circ}$. The evolution of the horizontal stresses at the bottom and at the top of the key block at the center of the immediate roof is plotted in Fig. 4A. While the horizontal stresses are slightly compressive before the tunnel block is removed, immediately after the removal of the tunnel at $t=5$ s the measurement point at the top of the block indicates high compression whereas the measurement point at the bottom of the block indicates tension, as would be expected from a block undergoing internal bending deformation under gravity. Moreover, careful analysis of NMM results can be used to trace the geometry of the compressive arch in the bending block and in the immediate roof (Fig. 4B), an issue that has been under considerable debate in the rock mechanics literature [21–23]. The vertical stress and vertical displacement evolution in the analyzed key block as obtained with the modified NMM are shown in Fig. 4 (C and D), respectively.

In order to demonstrate the applicability of the proposed excavation sequence modeling capability to field scale problems let us consider the case of the Zedekiah cave, a 40 m span and 25 m deep underground quarry excavated underneath the old city of Jerusalem more than 2000 years ago and still stands today unsupported. The specifics of this case study have been reported in detail elsewhere [24] and will not be repeated here, for brevity. The physical, mechanical, and numerical input parameters for NMM simulations are listed in Table 1. In Fig. 5 the deformation

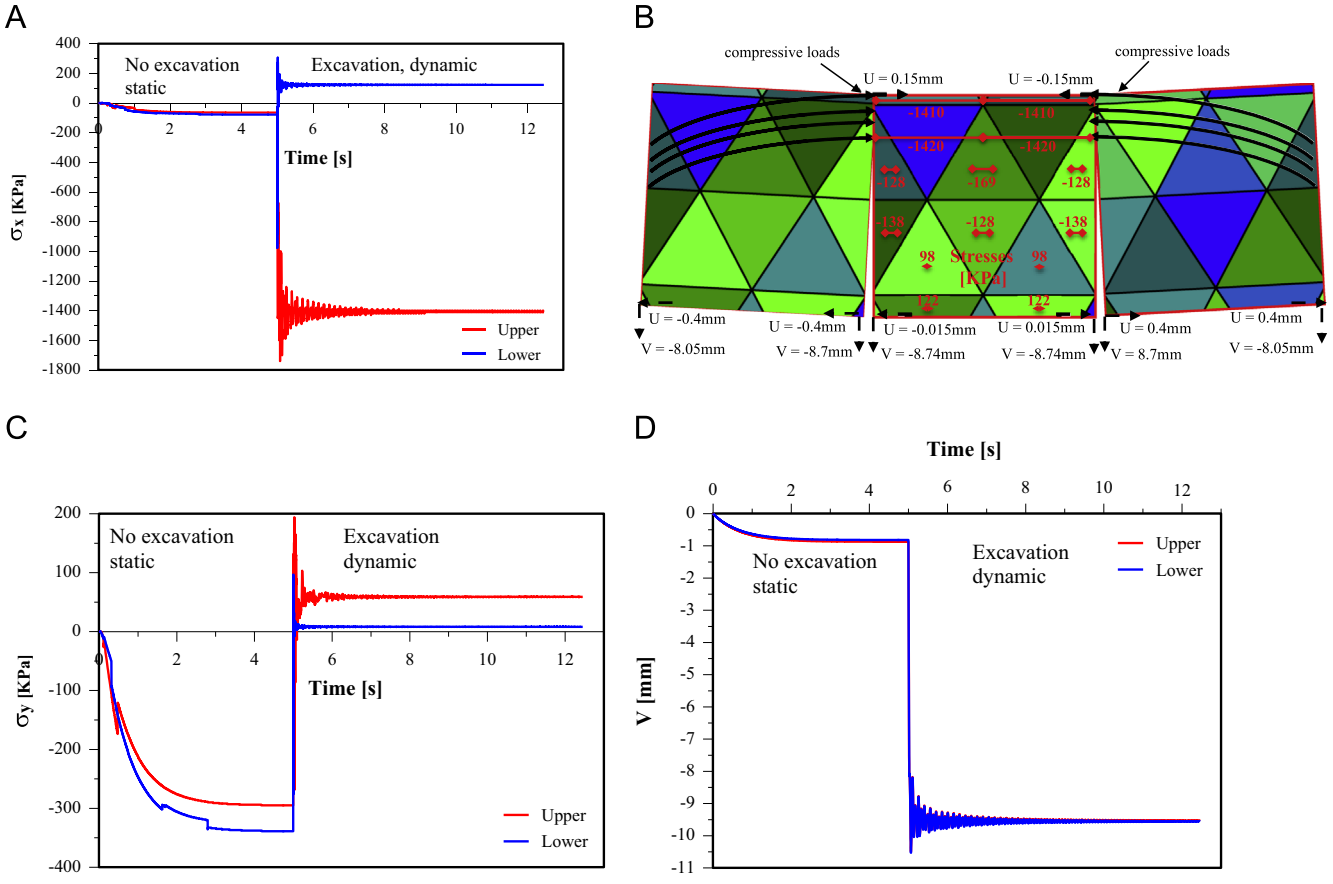

Fig. 4. Detailed analysis of single block deformation with modified NMM (for location see Fig. 3). (A) Horizontal stress evolution at the upper (red) and lower (blue) measurement points; (B) compressive arch thickness; vertical stress (C) and vertical displacement (D) evolution in analyzed block. (For interpretation of the references to color in this figure caption, the reader is referred to the web version of this paper.)

of the main hall in the cave is shown as obtained with the original (right panel) and modified (left panel) NMM. With the modified NMM the underground system attains stability with an available discontinuity friction angle of 15°, whereas with the original NMM a discontinuity friction angle of 25° is required, as can be inferred from the vertical displacement evolution of the immediate roof (Fig. 6). The result obtained with the modified NMM is supported by the fact that the main chamber of Zedekiah cave still stands unsupported today.

3. Imposing initial *in situ* stresses in NMM

When modeling deep underground excavations it is necessary to limit the modeled domain boundaries to the vicinity of the analyzed opening for better accuracy and computational efficiency. So that instead of letting the stresses evolve due to gravity from the ground level to the depth of interest, which could be several thousands of meters deep and therefore consume much needed CPU time in the process, the actual *in situ* stress field at the depth of interest can be imposed directly on the modeled domain. In the original NMM code developed by Shi [1] there is an option to specify the level of initial stresses ($\sigma_{xx,o}$, $\sigma_{yy,o}$, $\tau_{xy,o}$) which are applied everywhere in the modeled domain from the start of the analysis. When using this option we have found, however, that the user specified initial stresses in the original NMM code are not maintained at their original level throughout the analysis. Rather, they dissipate quite rapidly at the beginning of the simulation, for reasons not entirely clear to us. It is necessary to point out that we did not find the same problem in DDA. To overcome this problem we propose here an alternative method to impose initial *in situ* stresses in NMM.

The approach is aimed for deep underground excavations where the change in stresses due to gravity from top to bottom of the modeled domain may be assumed to be negligible with respect to the magnitude of the initial, far field stresses. Therefore, a homogenous stress distribution is assumed along the boundaries. To avoid rotations due to un-balanced moments the boundaries of the modeled domain are square. On each boundary, normal and tangential tractions are applied (Fig. 7).

Before we discuss our proposed boundary traction load algorithm for NMM we provide a brief summary of those NMM concepts and equations which are necessary for following our approach. A complete and detailed discussion of NMM theory is

Table 1
Input parameters for Zedekiah cave validation and Kirsch verification: *K*01 is the dynamic control parameter, *g*2 is assumed to be the maximum displacement ratio, *g*1 is the time step size, *g*0 is the stiffness of contact springs, *E* is Young's modulus, ν is Poisson's ratio and γ is the unit weight. The mesh density is defined as the higher number between the following two options: (1) the number of triangular element layers in half domain height or (2) the number of triangular elements in half domain width.

Case	*K*01	*g*2	*g*1 (s)	*g*0 (kN/m)	Mesh density	*E* (GPa)	ν	γ(kN/m^3)
Zedekiah cave	1	0.0001	0.00025	50×10^6	20	10	0.184	24.5
Kirsch	0	0.0005	0.001	100×10^6	52	25.3	0.22	0

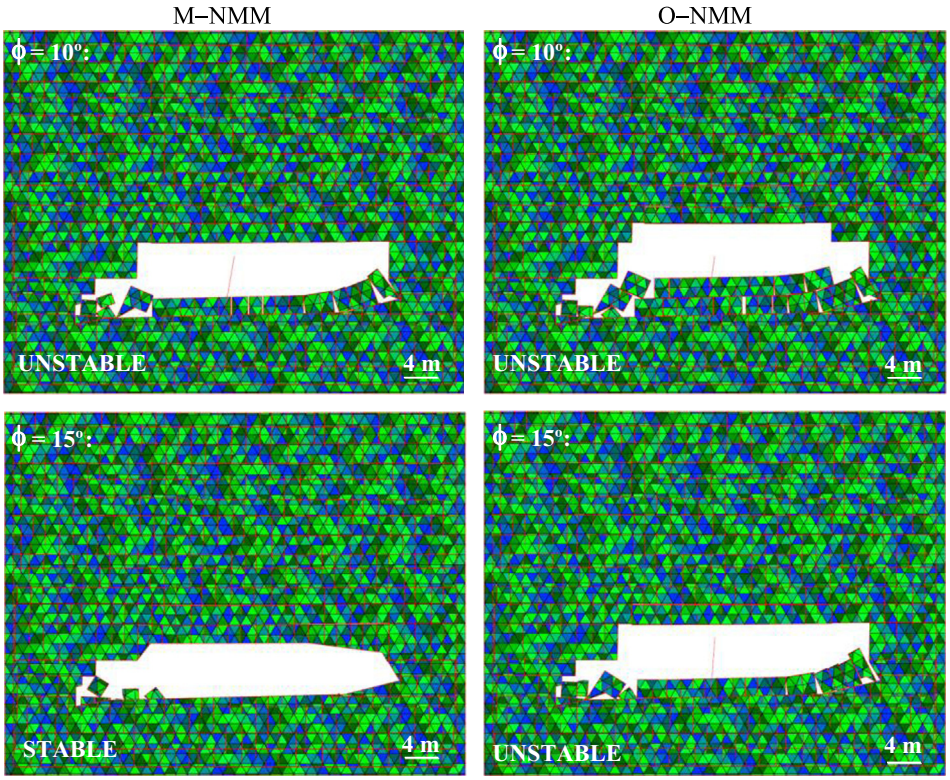

Fig. 5. Simulation of the case of Zedekiah cave [24] with the original (right) and modified (left) NMM for discontinuity friction angle of 10 and 15°.

provide by Shi [1]. Readers familiar with NMM theory can proceed directly to Section 3.2 without loss of continuity.

3.1. Brief review of cover, weighting, and displacement functions in NMM

The NMM finite cover system is based on three basic concepts: the mathematical cover, the physical cover, and the manifold element. The construction of mathematical covers, physical covers, manifold elements, and their associated functions are briefly reviewed below.

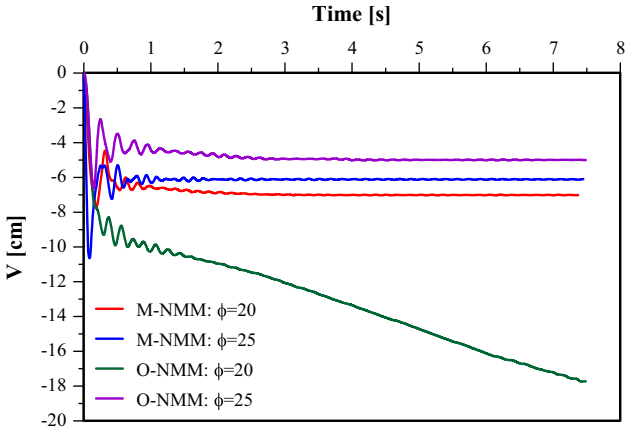

Fig. 6. The vertical displacement evolution of the immediate roof after the excavation showing that only when the available friction angle is 25° the cavern stabilizes with the original NMM.

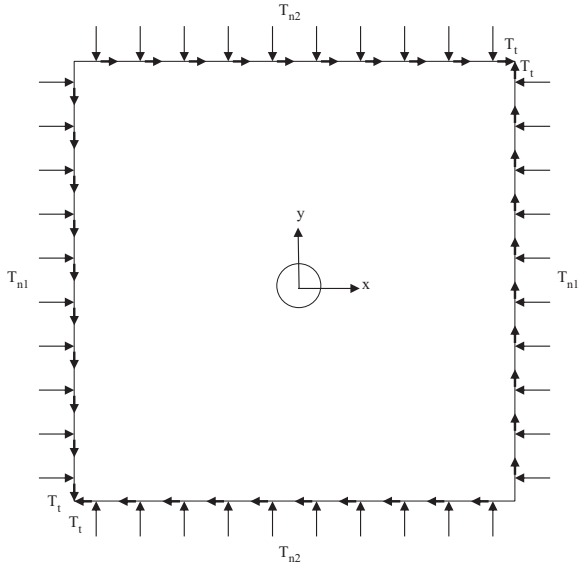

Fig. 7. Imposing *in situ* stresses by applying tractions on the plate boundaries.

3.1.1. Mathematical cover and weighting functions

Theoretically any shape of cover can be used in NMM. However, integration of manifold elements is related to the cover shape, and a reasonable choice of cover shape is very important [10]. A triangular finite element mesh is usually adopted to define the mathematical cover for manifold method. Therefore, mathematical cover that is based on triangular elements is discussed here.

A mathematical cover is a hexagonal composed of six triangular elements. The common node of the six triangular elements is regarded as a star. On each mathematical cover, a weight function w is defined. The weight function is equal to 1 in the center and declines linearly to zero at the sides of the mathematical cover, and has to satisfy

$$w_i(x,y) \geq 0, \quad (x,y) \in C_i$$
$$w_i(x,y) = 0, \quad (x,y) \notin C_i \tag{1}$$

$$\sum_{i=1}^{3} w_i(x,y) = 1, \quad (x,y) \in ME \tag{2}$$

where C_i is the mathematical cover and ME is a triangular element. Each triangular element (ME) is the common region of three mathematical covers ($M_{(i)}$, $i=1,2,3$) which are located in the triangular vertices. On each triangular element, the three weight functions of the mathematical covers are

$$w_{e(i)}(x,y) = \begin{matrix} w_{e(1)}(x,y) \\ w_{e(2)}(x,y) \\ w_{e(3)}(x,y) \end{matrix} = \frac{1}{\Delta} \begin{pmatrix} x_{(2)}y_{(3)} - x_{(3)}y_{(2)} & y_{(2)} - y_{(3)} & x_{(3)} - x_{(2)} \\ x_{(3)}y_{(1)} - x_{(1)}y_{(3)} & y_{(3)} - y_{(1)} & x_{(1)} - x_{(3)} \\ x_{(1)}y_{(2)} - x_{(2)}y_{(1)} & y_{(1)} - y_{(2)} & x_{(2)} - x_{(1)} \end{pmatrix} \begin{pmatrix} 1 \\ x \\ y \end{pmatrix} \tag{3}$$

where

$$\Delta = \begin{vmatrix} 1 & x_{(1)} & y_{(1)} \\ 1 & x_{(2)} & y_{(2)} \\ 1 & x_{(3)} & y_{(3)} \end{vmatrix} \tag{4}$$

is twice the area S of the element. Denote

$$\begin{pmatrix} f_{11} & f_{12} & f_{13} \\ f_{21} & f_{22} & f_{23} \\ f_{31} & f_{32} & f_{33} \end{pmatrix} = \frac{1}{2S} \begin{bmatrix} x_{(2)}y_{(3)} - x_{(3)}y_{(2)} & y_{(2)} - y_{(3)} & x_{(3)} - x_{(2)} \\ x_{(3)}y_{(1)} - x_{(1)}y_{(3)} & y_{(3)} - y_{(1)} & x_{(1)} - x_{(3)} \\ x_{(1)}y_{(2)} - x_{(2)}y_{(1)} & y_{(1)} - y_{(2)} & x_{(2)} - x_{(1)} \end{bmatrix} \tag{5}$$

then

$$w_{e(i)} = \begin{Bmatrix} w_{e(1)}(x,y) \\ w_{e(2)}(x,y) \\ w_{e(3)}(x,y) \end{Bmatrix} = \begin{pmatrix} f_{11} & f_{12} & f_{13} \\ f_{21} & f_{22} & f_{23} \\ f_{31} & f_{32} & f_{33} \end{pmatrix} \begin{Bmatrix} 1 \\ x \\ y \end{Bmatrix} = \begin{pmatrix} f_{11} + f_{12}x + f_{13}y \\ f_{21} + f_{22}x + f_{23}y \\ f_{31} + f_{32}x + f_{33}y \end{pmatrix} \tag{6}$$

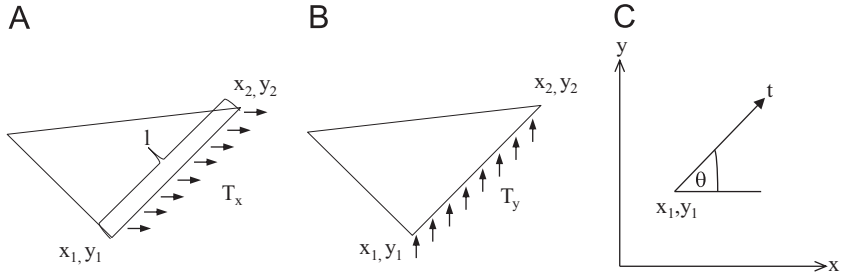

Fig. 8. Horizontal (A) and vertical (B) traction on an element's edge, and the projection of the edge on a global Cartesian coordinates (C).

3.1.2. Physical cover and weighting functions

The physical cover is the intersection of the mathematical cover and the material volume, and it inherits the weight function from its associate mathematical cover. In addition, on each physical cover, a local cover function is defined. The cover function can be constant, linear, high-order polynomial, or a local series. In the original NMM, however, a constant cover function is defined as

$$\begin{aligned} u &= u_i \\ v &= v_i \end{aligned} \tag{7}$$

If a mathematical cover is partially out of the physical cover, the weight function should be effective only in the region of the physical cover, and thus, a modifier, δ, is acting on the weight function

$$w_i(x,y) = \delta_i \cdot w_i(x,y) \tag{8}$$

where $\delta_i = 1$, within the problem domain, and $\delta_i = 0$ elsewhere.

3.1.3. Manifold elements and global displacement function

The elements of the manifold are the common regions of the physical covers, and thus, are also the common region of three stars. The linear weight function given in Eq. (3) and the constant local function given in Eq. (7) for each physical component in the manifold element are connected together to form a global linear displacement function for each manifold element which is given by the following equation:

$$\begin{Bmatrix} u(x,y) \\ v(x,y) \end{Bmatrix} = \begin{pmatrix} w_{e(1)}(x,y) & 0 & w_{e(2)}(x,y) & 0 & w_{e(3)}(x,y) & 0 \\ 0 & w_{e(1)}(x,y) & 0 & w_{e(2)}(x,y) & 0 & w_{e(3)}(x,y) \end{pmatrix} \begin{Bmatrix} u_{e(1)} \\ v_{e(1)} \\ u_{e(2)} \\ v_{e(2)} \\ u_{e(3)} \\ v_{e(3)} \end{Bmatrix} \tag{9}$$

where $e(1)$, $e(2)$, and $e(3)$ are the three star nodes of the manifold element.

Denote

$$[T_{e(i)}(x,y)] = \begin{pmatrix} w_{e(i)}(x,y) & 0 \\ 0 & w_{e(i)}(x,y) \end{pmatrix}$$

$$\{D_{e(i)}\} = \begin{pmatrix} u_{e(i)} \\ v_{e(i)} \end{pmatrix}, \quad i = 1,2,3 \tag{10}$$

then the displacement becomes

$$\begin{Bmatrix} u(x,y) \\ v(x,y) \end{Bmatrix} = [T_e]\{D_e\} \tag{11}$$

3.1.4. Global equations of equilibrium

The global equations of equilibrium are derived using a FEM style potential energy minimization. The total potential energy Π is the summation of all the potential energy sources: (1) strain energy, (2) initial stresses, (3) point load, (4) body load, (5) inertia force, (6) fixed points for the continuous material, (7) contact springs, and (8) friction forces for the discontinuities. The total potential energy for a problem with n star nodes can be expresses as follow:

$$\Pi = \frac{1}{2}\begin{Bmatrix} D_1^T & D_2^T & \dots & D_n^T \end{Bmatrix}\begin{pmatrix} K_{11} & K_{12} & \dots & K_{1n} \\ K_{21} & K_{22} & \dots & K_{2n} \\ \vdots & \vdots & \ddots & \vdots \\ K_{n1} & K_{n2} & \dots & K_{nn} \end{pmatrix}\begin{Bmatrix} D_1 \\ D_2 \\ \vdots \\ D_n \end{Bmatrix} + \begin{Bmatrix} D_1^T & D_2^T & \dots & D_n^T \end{Bmatrix}\begin{Bmatrix} F_1 \\ F_2 \\ \vdots \\ F_n \end{Bmatrix} + C \tag{12}$$

where $\{D_i\}$ is a 2×1 sub-vector of the displacements $(u_i\ v_i)$ of a star node, $[K_{ij}]$ is the coefficient 2×2 sub-matrix, and $\{F_i\}$ is 2×1 loading sub-vector. Minimizing the total potential energy Π, the global equations of equilibrium are the following:

$$\begin{pmatrix} K_{11} & K_{12} & \cdots & K_{1n} \\ K_{21} & K_{22} & \cdots & K_{2n} \\ \vdots & \vdots & \ddots & \vdots \\ K_{n1} & K_{n2} & \cdots & K_{nn} \end{pmatrix}\begin{Bmatrix} D_1 \\ D_2 \\ \vdots \\ D_n \end{Bmatrix} = \begin{Bmatrix} F_1 \\ F_2 \\ \vdots \\ F_n \end{Bmatrix} \tag{13}$$

3.2. Inserting tractions to NMM

From Cauchy's stress theorem, the traction on each boundary plane is

$$\tau_i = \sigma_{ij} n_j \tag{14}$$

where σ_{ij} is the stress tensor and n_j is the normal to the plane. In addition to the tractions on the boundaries, the existing "initial stress" option in NMM is also applied in each element in the modeled domain, with the same values as the *in situ* stresses that are applied on the boundaries using the new "traction load" option.

With this procedure there should not be any displacement or rotations before the excavation as the initial medium stresses are identical to the tractions on the boundaries so that the system is at equilibrium. Because in a numerical method small displacements and rotation may still occur, the plate is also constrained by fixed boundaries around it utilizing the existing "fixed point" option in the original NMM code.

At the element scale (Fig. 8), horizontal (A) and vertical (B) tractions can act on an element edge which is also a physical boundary. The potential energy due to constant tractions on the element boundary is the following:

$$\Pi_T = -\int_t (u(x.y)\ v(x.y))\begin{Bmatrix} T_x \\ T_y \end{Bmatrix} dt = -\{D_e\}^T\left[\int_t [T_e(x,y)]dt\right]\begin{Bmatrix} T_x \\ T_y \end{Bmatrix} \tag{15}$$

where $\{T_x \quad T_y\}^T$ is a constant traction acting on the boundary of element *ME*, and t is the coordinate along the edge starting from vertex (x_1,y_1) (see Fig. 8c). Substituting Eqs. (6) and (10), the potential energy becomes

$$\begin{aligned} \Pi_T &= -\{D_e\}^T\left[\int_t \begin{bmatrix} w_{e(i)}(x,y) & 0 \\ 0 & w_{e(i)}(x,y) \end{bmatrix} dt\right]\begin{Bmatrix} T_x \\ T_y \end{Bmatrix} \\ &= -\{D_e\}^T\left[\int_t \begin{bmatrix} f_{r1}+f_{r2}x+f_{r3}y & 0 \\ 0 & f_{r1}+f_{r2}x+f_{r3}y \end{bmatrix} dt\right]\begin{Bmatrix} T_x \\ T_y \end{Bmatrix}, \\ r &= 1,2,3 \end{aligned} \tag{16}$$

The relation between the coordinate of an element edges (x_1,y_1) and the global coordinate system (x,y) is as follows:

$$x = x_1 + t\ \cos\ \theta$$
$$y = y_1 + t\ \sin\ \theta \tag{17}$$

and therefore

$$\begin{aligned}\Pi_T &= -\{D_e\}^T\left[\int_t \begin{bmatrix} f_{r1}+f_{r2}(x_1+t\ \cos\ \theta)+f_{r3}(y_1+t\ \sin\ \theta) & 0 \\ 0 & f_{r1}+f_{r2}(x_1+t\ \cos\ \theta)+f_{r3}(y_1+t\ \sin\ \theta)\end{bmatrix} dt\right]\begin{Bmatrix} T_x \\ T_y\end{Bmatrix} \\ &= -\{D_e\}^T\begin{bmatrix} f_{r1}t+f_{r2}\left(x_1+\frac{t}{2}\ \cos\ \theta\right)t+f_{r3}\left(y_1+\frac{t}{2}\ \sin\ \theta\right)t & 0 \\ 0 & f_{r1}t+f_{r2}\left(x_1+\frac{t}{2}\ \cos\ \theta\right)t+f_{r3}\left(y_1+\frac{t}{2}\ \sin\ \theta\right)t\end{bmatrix}_0^l\begin{Bmatrix} T_x \\ T_y\end{Bmatrix} \\ &= -\{D_e\}^T\begin{bmatrix} f_{r1}l+f_{r2}\left(x_1+\frac{l}{2}\ \cos\ \theta\right)l+f_{r3}\left(y_1+\frac{l}{2}\ \sin\ \theta\right)l & 0 \\ 0 & f_{r1}l+f_{r2}\left(x_1+\frac{l}{2}\ \cos\ \theta\right)l+f_{r3}\left(y_1+\frac{l}{2}\ \sin\ \theta\right)l\end{bmatrix}\begin{Bmatrix} T_x \\ T_y\end{Bmatrix}\end{aligned} \tag{18}$$

where the length of the edge (l), $\cos\theta$ and $\sin\theta$ can be expressed as follows:

$$l = \sqrt{(y_2-y_1)^2+(x_2-x_1)^2}$$
$$\cos\ \theta = \frac{x_2-x_1}{l}$$
$$\sin\ \theta = \frac{y_2-y_1}{l} \tag{19}$$

Therefore,

$$\begin{bmatrix} f_{r1}+f_{r2}\left(x_1+\frac{l}{2}\ \cos\ \theta\right)+f_{r3}\left(y_1+\frac{l}{2}\ \sin\ \theta\right) & 0 \\ 0 & f_{r1}+f_{r2}\left(x_1+\frac{l}{2}\ \cos\ \theta\right)+f_{r3}\left(y_1+\frac{l}{2}\ \sin\ \theta\right)\end{bmatrix}\cdot l\begin{Bmatrix} T_x \\ T_y\end{Bmatrix} \tag{20}$$
$$\downarrow$$
$$\{F_{e(r)}\},\quad r=1,2,3$$

is the element (6×1) traction loading vector composed of 3 (2×1) vectors which are assembled into the global loading vector $\{F_e\}$ according to the element's nodes.

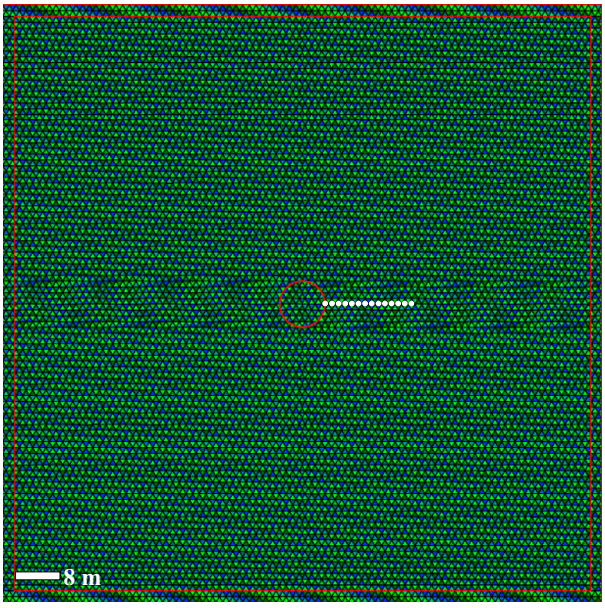

Fig. 9. NMM model of a continuous elastic plate with a circular hole in its center (red circle) before the excavation. The measurement points are drawn in white. (For interpretation of the references to color in this figure caption, the reader is referred to the web version of this paper.)

3.3. Verifications using Kirsch solution

Kirsch solution [25] assumes continuous, homogeneous, linear elastic medium and is typically used in deep tunneling applications where the change of the vertical stress with depth due to gravity is negligible relatively to the *in situ* stress level. Therefore, we use Kirsch solution to verify both the sequential excavation and the imposed traction algorithms using the model geometry shown in Fig. 9.

The mechanical parameters of the medium and the numerical parameters in the simulation are presented in Table 1. The radius of the hole (a) is 4 m. The *in situ* stresses ($\sigma_{xx}=-5$ MPa, $\sigma_{yy}=-10$ MPa, and $\tau_{xy}=1$ MPa) are imposed on the plate as initial stresses at the beginning of the simulation, and additionally, tractions are acting on the boundaries during the entire simulation. Fig. 10 shows the horizontal, vertical and shear stresses at the last time step before the excavations. In all cases, the stresses in the modeled domain fit very well to the desired *in situ* stresses.

The comparisons between analytically derived and numerically obtained stresses once the excavation is performed are shown in Fig. 11 as a function of distance from the center of the cavity. Note that the measurement points are not located at the direction of the principle stresses ($\theta=-10.9^\circ$) and that the analytical solutions for the stresses and displacements are calculated accordingly. The agreement between the analytical and numerical solutions is determined by the numerical relative error, which is defined in

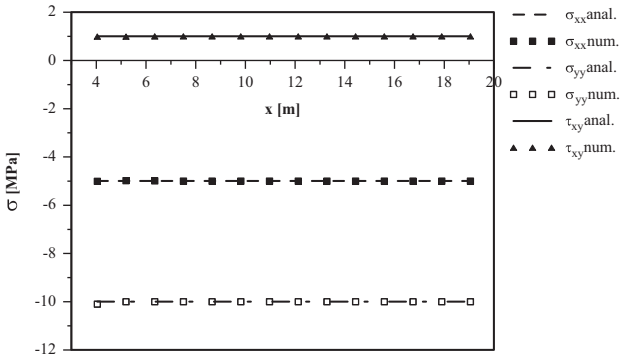

Fig. 10. The horizontal, vertical and shear stresses at the last time step before the excavations as a function of the horizontal distance from center of the hole (see Fig. 9).

a conventional manner as

$$E_N = \left|\frac{d - d_N}{d}\right| \cdot 100 \quad (21)$$

where d and d_N are analytical and numerical solutions, respectively.

A good agreement is obtained between the numerical and analytical results. The relative errors for the horizontal stress declines with increasing distance from the center of the hole: from 93% at the nearest point (1.01 radii) where the stress is very small and therefore the relative error is high, to 6.7% at the second point (1.3 radii), to 0.6% at all points beyond two radii from the center of the hole. Similarly, the relative error for the vertical stress declines with increasing distance from the center of the hole: from 9% to 1.5% at all points which are located more than two radii from the center of the hole. Comparison between analytically derived and numerically obtained horizontal displacement (U) is also shown in Fig. 11. A good agreement is obtained, but because the horizontal displacement decreases significantly with increasing distance from the center of the hole to very small values in the order of 0.01 mm, the relative errors increase (as per Eq. 14 where a small d increases E_N) from 6% at the nearest point to 10–20% between 1.3 radii and 2.2 radii, to 20–200% above 2.5 radii.

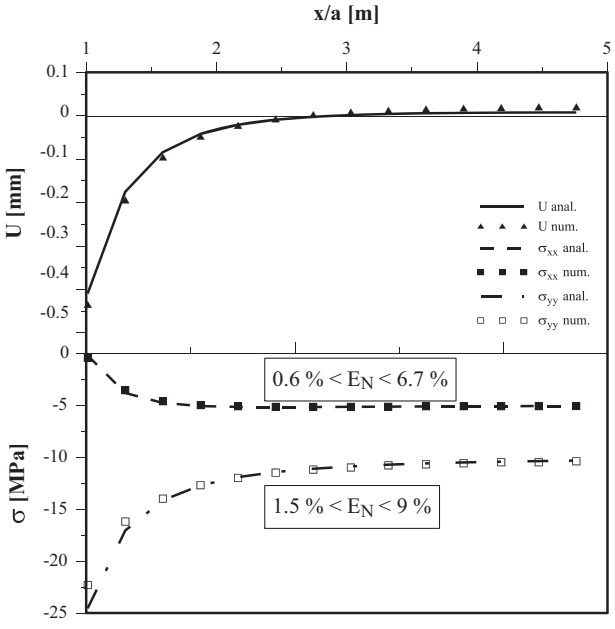

Fig. 11. Comparison between NMM and Kirsch solution: vertical (σ_{yy}) and horizontal (σ_{xx}) stresses and horizontal displacements (U) as a function of the horizontal distance from the center of the hole normalized by the hole's radius.

We may safely conclude therefore that the two enhancements performed by us to NMM work well, and we can proceed with application to a real case study.

4. Stress inversion in Jinping tunnels using *in situ* displacement measurements and modified NMM

4.1. *In situ* displacement monitoring at Jinping

To demonstrate the applicability of the NMM modifications presented here we use the modified NMM code to resolve the *in situ* stress field at the deep tunnels of Jinping hydroelectric project located in Sichuan province, China, using sliding micrometer data obtained in an exploratory borehole by Li et al. [26], during ongoing excavation and consequent strain relaxation of the rock mass at the side wall of a newly created research tunnel.

The Jinping 4800 MW hydro-electrical project involves the construction of four headrace tunnels under a maximum overburden of up to 2525 m. The question of the exact magnitude of the principal stresses at the tunnels' depth has been an issue of considerable debate (e.g. [27–30]), particularly since *in situ* testing did not provide conclusive and consistent results. A prediction of the macro-distribution of *in situ* stress axes along the headrace tunnels of the Jinping II Hydropower Station has been suggested by Zhang et al. [31] and is shown in Fig. 12. Here we attempt to resolve the magnitude of the three stress components (σ_{xx}, σ_{zz}, τ_{xz}) in a two-dimensional cross section normal to the tunnel axis at the

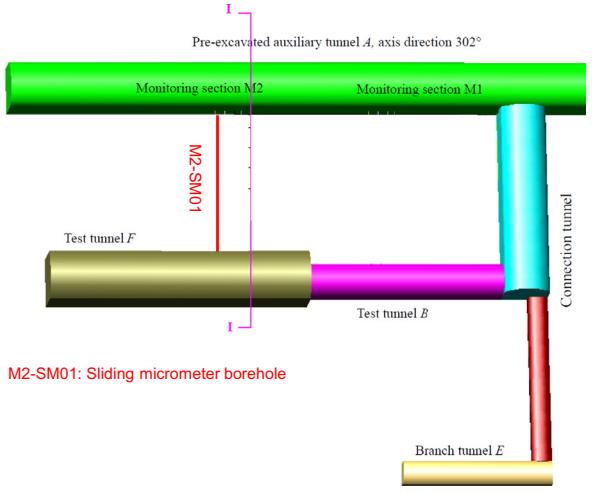

Fig. 13. Layout of *in situ* monitoring campaign performed by Li et al. [26] in Jinping test tunnels *F* and *B*. Sliding micrometer data were obtained in borehole labeled M2-SM01 (modified after Li et al. [26]).

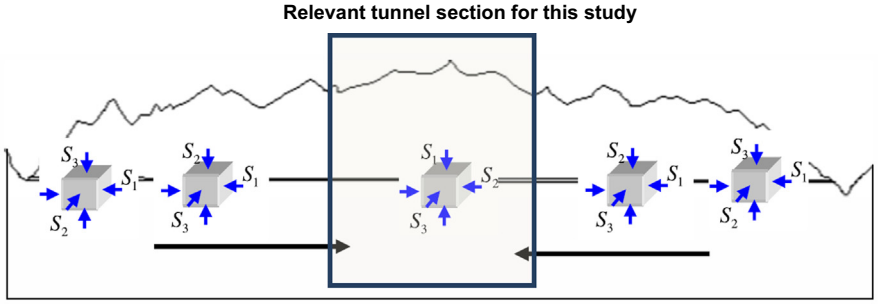

Fig. 12. Prediction of the macro-distribution of *in situ* stress along the headrace tunnels of the Jinping II Hydropower Station (modified after Zhang et al. [31]). Relevant tunnel section to the stress inversion analysis performed here is shaded.

deepest segments of the headrace tunnels. In our coordinate system, the *x*-axis is horizontal and normal to the tunnel axis, and the *z*-axis is vertical.

Li et al. [26] performed high precision displacement monitoring *in situ* using the sliding micrometer technique [32]. From an existing auxiliary tunnel (tunnel *A* in Fig. 13) they drilled a 23.7 m long, 110 mm diameter, exploratory borehole at an inclination of −2° (borehole M2-SM01 in Fig. 13) into the expected trajectory of a test tunnel labeled *F* in Fig. 13. Twenty-two measurement points were positioned inside the borehole at 1 m intervals and the annular space between the tubes and borehole wall was grouted. To avoid interferences due to construction related activities in auxiliary tunnel *A*, the reference point in the borehole was selected at a distance of 4 m from the free face of tunnel *A*. Therefore, 17 measurement points could be used for inversion; a typical output of the sliding micrometer displacement data obtained by [26] for the monitored period of November 30, 2009 to January 10, 2011 is shown in Fig. 14. The high precision sliding micrometer data [32] obtained by Li et al. [26] provide the response of the rock mass to the excavation of test tunnel *F* (Fig. 13) and are used here, therefore, to perform the stress inversion.

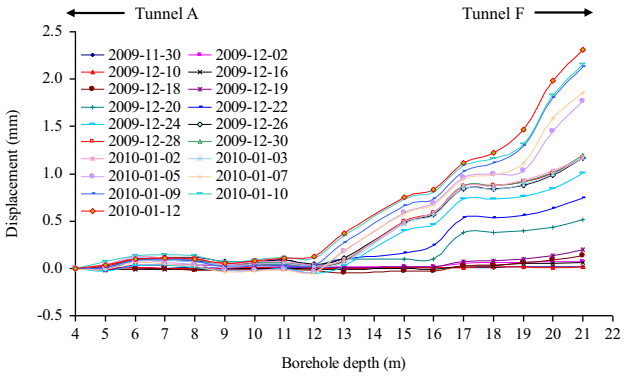

Fig. 14. Typical output of the sliding micrometer data obtained in borehole M2-SM01 during excavation of test tunnel *F* (modified after Li et al. [26]).

4.2. Stress inversion for Jinping tunnels using sliding micrometer data

In order to find the *in situ* stress at the site by inversion, the excavation sequence of auxiliary tunnel *A* and test tunnel *F* (see Fig. 14) is first modeled with the modified NMM code. The displacements of 17 measurement points along a trace line parallel to borehole M2-SM01 obtained by NMM simulations for a range of far field, initial, *in situ* stress values (σ_{xx}, σ_{zx}, τ_{xz}) are compared with the equivalent sliding micrometer displacement data measured in the field in borehole M2-SM01, in order to achieve the best fit between the numerical and measured displacements.

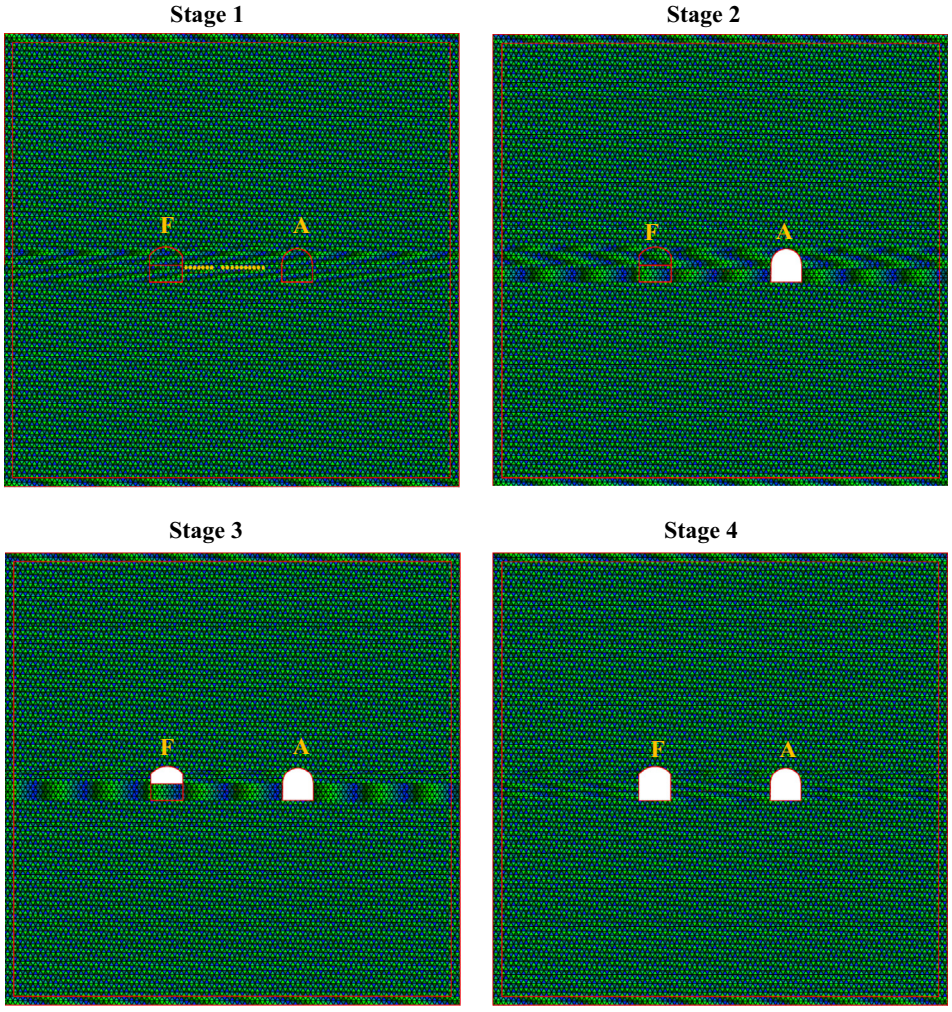

Fig. 15. Four stages of excavation sequence modeling with NMM in the Jinping project. Measurement point locations are shown in upper left panel.

The magnitude of the vertical stress is considered a known quantity as it is assumed to be generated by overburden stress only; we therefore assume a value of $\sigma_{zz} = -66.5$ MPa in our simulations, following Li et al. [26] (here compression is negative). Similarly, the values of Young's modulus ($E = 25.3$ GPa) and Poisson's ratio ($\nu = 0.22$) are taken from Li et al. [26] and are kept constant through all simulations. We vary the unknown horizontal stress component (σ_{xx}) between -10 and -70 MPa and the unknown shear stress component (τ_{xz}) between -10 and 10 MPa between the NMM simulations. Hence, 651 NMM simulations with different combinations of σ_{xx} and τ_{xz} are performed automatically by a self-developed C program.

All simulations are performed under plane strain boundary condition and include four stages (Fig. 15): in stage 1 both tunnels are closed, *in situ* stresses are acting on the boundaries, and initial stresses exist everywhere in the domain. Then, after the stresses are stable and the domain is organized with small initial displacements, auxiliary tunnel *A* is removed at stage 2. At stages 3 and 4 the top heading and bench of tunnel *F* are removed, respectively. Seventeen measurement points are located in the NMM model (see Fig. 15) to measure the displacements during the simulation. The location of the measurement points in the model is exactly identical to their locations in borehole M2-SM01 in the field. Since borehole M2-SM01 was drilled after auxiliary tunnel *A* was excavated, only the displacements during stages 3 and 4 in the simulation are compared with the measured displacements in the field (shown in Fig. 14).

In order compare displacement in 17 measurement points taking into consideration the effect of all of them simultaneously, the root mean square (d_{RMS}) of the displacements in each simulation is calculated. The d_{RMS} gives the same weight for each measurement point since it does not include relative values, and is defined as

$$d_{RMS} = \sqrt{\frac{(d_1 - d_{N1})^2 + (d_2 - d_{N2})^2 + \cdots + (d_n - d_{Nn})^2}{n}} \quad (22)$$

where d_i and d_{Ni} are measured and numerical solutions of the *i*th measurement point, respectively, and n is the amount of measurement points.

Fig. 16 shows the d_{RMS} of the displacements as a function of the horizontal and shear stress components within the varied range of values. Inspection of the results reveals that the d_{RMS} is very sensitive to the value of the horizontal stress with a distinct minimum ($d_{RMS} < 0.5$ mm) at values between -30 and -36 MPa, while the sensitivity of the results to the exact value of the shear stress is less pronounced. Nevertheless, we are also able to constrain the best fit shear stress value:, as clearly shown in Fig. 16, only with a pair of far field stress values of $\sigma_{xx} = -34$ MPa and $\tau_{xz} = -8$ MPa, the obtained d_{RMS} value is smaller than 0.25 mm ($d_{RMS} = 0.24$ mm). The displacement results of the 17 measurement points under the best fit far field stress solution obtained above ($\sigma_{xx} = -34$ MPa, $\sigma_{zz} = -66.48$ MPa, and $\tau_{xz} = -8$ MPa) is shown in Fig. 17.

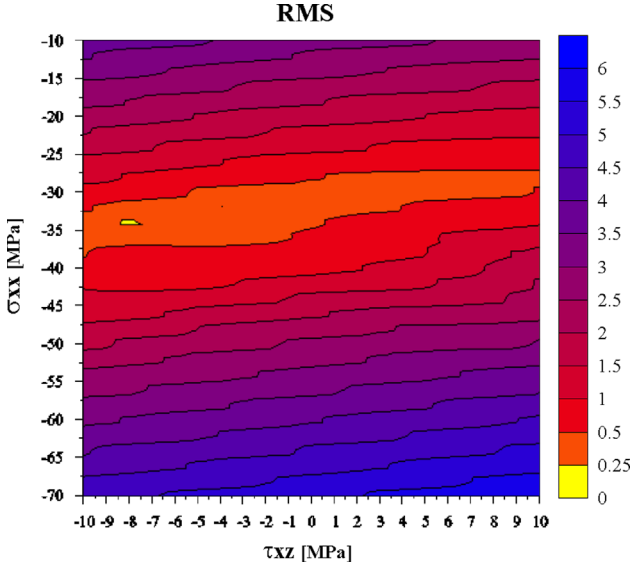

Fig. 16. d_{RMS} (mm) of the displacements of all measurement points during the excavation of tunnel *F* (both parts) as a function of σ_{xx} and τ_{xz} (651 simulations).

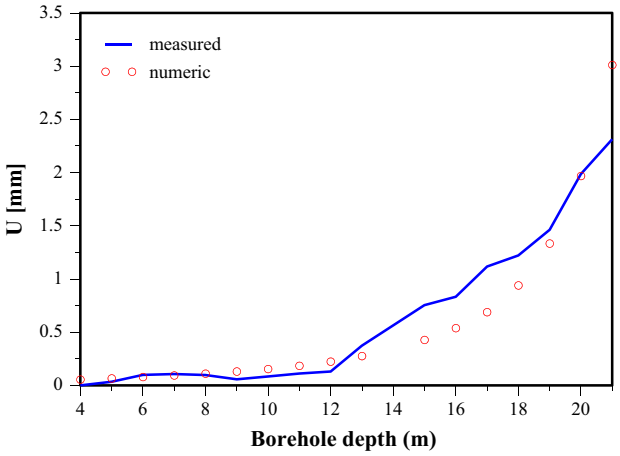

Fig. 17. Displacements at all measurement points during the excavation of tunnel *F* (both parts) as a function of borehole depth for the simulation with stress values of $\sigma_{xx} = -34$ MPa, $\sigma_{zz} = -66.48$ MPa, and $\tau_{xz} = -8$ MPa.

4.3. Principal stresses at Jinping tunnels based on stress inversion

Having obtained the best fit *in situ* stress field (σ_{xx}, σ_{zz}, τ_{xz}) for the analyzed section in Jinping tunnels by inversion of sliding micrometer data, we can now determine the principal stresses in the analyzed cross section by two-dimensional stress transformation. The resulting principal stresses thus obtained are $\sigma_1 = -68.35$ MPa and $\sigma_2 = -32.14$ MPa. The direction of the principal stresses in the analyzed cross section is $\theta = -13.1^\circ$, namely the major principal stress is sub-vertical and the minor principal stress is sub-horizontal, dipping at 13.1° to the north (see Fig. 18).

Recall that the two-dimensional numerical analysis with NMM was performed under an assumed plain strain boundary condition. This assumption constrains further the value of the minor principal stress σ_3. Re-writing Hoek's law in terms of principal stresses for the special case of plain strain, the minimum principal stress σ_3 is given by

$$\sigma_3 = \nu(\sigma_1 + \sigma_2) \quad (23)$$

With a Poisson's ratio of $\nu = 0.22$ this implies a minimum principal stress of $\sigma_3 = -22.11$ MPa acting horizontally parallel to the tunnel axis, assuming that the analyzed cross section is a principal plane.

It is important to realize that the value of the principal stress parallel to the tunnel axis obtained here assuming plain strain boundary conditions does not reflect the possible effect of *in situ* tectonic stresses, believed to be quite high in that direction in the field [31], as its magnitude is generated by the elastic response due to Poisson's effect under the imposed plain strain boundary condition. Therefore, the actual value of the principal stress parallel to the tunnel axis is still not resolved here, as well as its

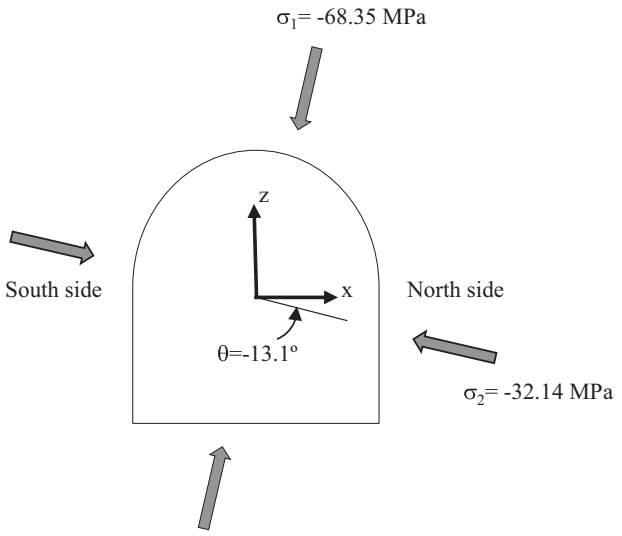

Fig. 18. The principle stresses at the tunnel section (plane x–z) obtained by the transformation of normal and shear stresses obtained by inversion of the sliding micrometer displacement data.

relationship to the other two principal stresses determined here by inversion of displacement data.

5. Summary and conclusions

We modify here the original NMM code developed by Shi [1] to improve numerical investigations of underground structures by introducing the following two enhancements:

1. We develop a new boundary condition that allows accurate application of initial stresses in deep tunnels by inserting constant tractions that are acting on the boundary of a manifold element.
2. We develop excavation sequence modeling capabilities in NMM by enabling the removal of tunnels of any shape during ongoing computation.

The modified code is verified using existing analytical solutions.

We demonstrate the significance of modeling excavation sequence by means of the Zedekiah cave case study, a shallow and wide span underground quarry below the old city of Jerusalem excavated in horizontally layered and vertically jointed limestone. While with the original NMM code the required friction angle for stability is 25°, with the modified NMM code a friction angel of 15° is shown to be sufficient to stabilize the modeled cavern. We conclude therefore that using the original NMM may lead to an overly conservative design.

The initial stress enhancement performed in the NMM code by inserting tractions on element boundaries is used to resolve the *in situ* stress field in Jinping tunnels by inversion of displacement data measured *in situ* during ongoing construction using the sliding micrometer technique. By keeping the vertical stress constant the best fit horizontal and shear stress components are found from the least root mean square error between the numerical and measured results of 17 measurement points. With an assumed vertical stress of -66.48 MPa, the best fit is achieved with a horizontal stress value of -34 MPa and a shear stress value of -8 MPa in the plane which is normal to the tunnel axis. Using simple two-dimensional stress transformation, the principal stresses in the tunnel section are: $\sigma_1=-68.35$ MPa, $\sigma_2=-32.14$ MPa and their direction is $\theta=-13.1°$.

Acknowledgments

This research is jointly funded by Israel Science Foundation through grant ISF-2201 contract No. 556/08, and by the Chinese Academy of Sciences through a visiting professorship grant for Senior International Scientists (No. 2011T2G29) awarded to Y. Hatzor in 2011. Dr. Shi Gen-hua is thanked for sharing his original source code of NMM and for fruitful discussions. Drs. Li Shaojun, Quan Jiang, and Chen Bingrui from the State Key Laboratory of Geomechanics and Geotechnical Engineering, Institute of Rock and Soil Mechanics, CAS, Wuhan, are thanked for sharing their in-situ monitoring data, field trips, and stimulating discussions.

References

[1] Shi GH. Manifold method. In: Proceedings of the first international forum on discontinuous deformation analysis (DDA) and simulations of discontinuous media. Albuquerque, New Mexico, USA: TSI Press; 1996a. p. 52–204.
[2] Shi GH. Discontinuous deformation analysis—a new numerical method for the statics and dynamics of block system [PhD Thesis]. UC Berkeley; 1988.
[3] MacLaughlin MM, Doolin DM. Review of validation of the discontinuous deformation analysis (DDA) method. Int J Numer Anal Meth Geomech 2006;30:271–305.
[4] Wu JH, Ohnishi Y, Nishiyama S. Simulation of the mechanical behavior of inclined jointed rock masses during tunnel construction using Discontinuous Deformation Analysis (DDA). Int J Rock Mech Min Sci 2004;41:731–43.
[5] Tsesarsky M, Hatzor YH. Tunnel roof deflection in blocky rock masses as a function of joint spacing and friction—a parametric study using discontinuous deformation analysis (DDA). Tunnell Underg Space Tech 2006;21:29–45.
[6] Zuo JP, Peng SP, Li YJ, Chen ZH, Xie HP. Investigation of karst collapse based on 3-D seismic technique and DDA method at Xieqiao coal mine, China. Int J Coal Geol 2009;78:276–87.
[7] Zhao ZY, Zhang Y, Bao HR. Tunnel blasting simulations by the discontinuous deformation analysis. Int J Comp Meth 2011;8:277–92.
[8] Jiang QH, Wei W, Yao C, Zhou CB. Failure mode analysis of jointed rock masses around underground opening under excavation unloading. Maters Res Innov 2011;15:609–12.
[9] Jing L. A review of techniques, advances and outstanding issues in numerical modelling for rock mechanics and rock engineering. Int J Rock Mech Min Sci 2003;40:283–353.
[10] Chen GQ, Ohnishi Y, Ito T. Development of high-order manifold method. Int J Numer Meth Eng 1998;43:685–712.
[11] Cheng Y, Li S, Wu YF. Numerical manifold method based on the method of weighted residuals. Comput Mech 2005;35:470–80.
[12] Cheng YM, Zhang YH. Formulation of a three-dimensional numerical manifold method with tetrahedron and hexahedron elements. Rock Mech Rock Eng 2008;41:601–28.
[13] Jiang QH, Zhou CB, Li DQ. A three-dimensional numerical manifold method based on tetrahedral meshes. Comput Struct 2009;87:880–9.
[14] Ma GW, An XM, He L. The numerical manifold method: a review. Int J Comput Meth 2010;7:1–32.
[15] Chiou YJ, Lee YM, Tsay RJ. Mixed mode fracture propagation by manifold method. Int J Fract 2002;114:327–47.
[16] Tsay RJ, Chiou YJ, Chuang WL. Crack growth prediction by manifold method. J Eng Mech 1999;125:884–90.
[17] He L, Ma GW. Development of 3d numerical manifold method. Int J Comput Meth 2010;7:107–29.
[18] Hatzor YH, Wainshtein I, Bakun Mazor D. Stability of shallow karstic caverns in blocky rock masses. Int J Rock Mech Min Sci 2010;47:1289–303.
[19] MacLaughlin M, Sitar N. A gravity turn-on routine for DDA. In: Third international conference on analysis of discontinuous deformation (ICADD-3) VAIL, Colo; June 3–4, 1999, p. 65–74.
[20] Jiang Q, Zhou C, Li D, Yeung M. A softening block approach to simulate excavation in jointed rocks. Bull Eng Geol Environ 2012;71:747–59.
[21] Sofianos I. Analysis and design of an underground hard rock Voussoir beam roof. Int J Rock Mech Min Sci 1996;33:153–66.
[22] Diederichs MS, Kaiser PK. Stability of large excavations in laminated hard rock masses: the voussoir analogue revisited. Int J Rock Mech Min Sci 1999;36:97–117.
[23] Tsesarsky M, Talesnick ML. Mechanical response of a jointed rock beam—numerical study of centrifuge models. Int J Numer Anal Meth Geomech 2007;31:977–1006.
[24] Bakun-Mazor D, Hatzor YH, Dershowitz WS. Modeling mechanical layering effects on stability of underground openings in jointed sedimentary rocks. Int J Rock Mech Min Sci 2009;46:262–71.
[25] Kirsch G. Die theorie der elastizitat und die bedurfnisse der festigkeitslehre. Veit Ver Deut Ing 1898;42:797–807.
[26] Li S, Feng XT, Li Z, Chen B, Zhang C, Zhou H. *In situ* monitoring of rockburst nucleation and evolution in the deeply buried tunnels of Jinping II hydropower station. Eng Geol 2012;137 and 138:85–96.

[27] Gong M, Qi S, Liu J. Engineering geological problems related to high geo-stresses at the Jinping I Hydropower Station, Southwest China. Bull Eng Geol Environ 2010;69:373–80.
[28] Qian QH, Zhou XP, Yang HQ, Zhang YX, Li XH. Zonal disintegration of surrounding rock mass around the diversion tunnels in Jinping II Hydropower Station, Southwestern China. Theor Appl Fract Mech 2009;51:129–38.
[29] Zhang CQ, Zhou H, Feng XT. An index for estimating the stability of brittle surrounding rock mass: FAI and its engineering application. Rock Mech Rock Eng 2011;44:401–14.
[30] Ge XR, Hou MX. Principle of *in-situ* 3D rock stress measurement with borehole wall stress relief method and its preliminary applications to determination of *in-situ* rock stress orientation and magnitude in Jinping hydropower station. Sci China Tech Sci 2012;55:939–49.
[31] Zhang CQ, Feng XT, Zhou H. Estimation of *in situ* stress along deep tunnels buried in complex geological conditions. Int J Rock Mech Min Sci 2012;52:139–62.
[32] Kovari K, Amstad C, Koppel J. New developments in the instrumentation of underground openings. In: Proceedings of the fourth rapid excavation and tunnelling conference, Atlanta, USA; June 18–21 1979. p. 817–37.